Chapter 5: Stabilization of the Premartensite Phase in $Ni_{50}Mn_{34}In_{16-x}Al_x$ (x = 0.5, 0.8) Magnetic Shape Memory Alloys

This chapter presents the evidence for chemical pressure-induced suppression of the martensite transition and stabilization of the premartensite phase over a wide temperature range (~300 to 5 K) in $Ni_{50}Mn_{34}In_{16}$ (or $Ni_2Mn_{1.36}Al_{0.64}$) magnetic shape memory alloy using magnetic susceptibility and synchrotron x-ray powder diffraction studies.

5.1 Introduction

Large shape change under the influence of external stress and its recovery on annealing above a characteristic temperature is the key property of a class of functional materials named shape memory alloys (SMAs) [16, 27, 106, 342]. The origin of the large recoverable shape change (strain) in SMAs is intimately linked with a diffusionless martensite phase transition in which a higher symmetry cubic austenite phase transforms to a lower symmetry martensite phase with tetragonal/orthorhombic/monoclinic Bain distortion [14, 15, 343]. The martensite transition in SMAs is a reversible transition, unlike in the steels where it is irreversible [344]. An interesting precursor or premartensite (PM) transition has been reported to precede the martensite phase transition in some of the SMAs [105, 106, 345]. This phenomenon and its role on the structure-property correlations in various SMAs has since been extensively investigated [105-111]. The precursor PM phase occurs at an intermediate temperature range between the high-temperature austenite and low-temperature martensite phase with preserved cubic symmetry of the austenite phase [105-111].

In recent years, the appearance of the PM phase has received considerable attention in another class of SMAs, known as magnetic shape memory alloys (MSMAs) [63, 83, 88, 97, 100-104]. The

advantage of the MSMAs over the SMAs is that the magnetic field-induced shape change is accompanied with much larger strain (MFIS) which can be recovered within the martensite phase itself without any annealing above the transition temperature [1, 3]. Also, the response time associated with the occurrence of the magnetic field-induced strain and its recovery is much faster than that in the conventional SMAs [1], opening the possibility for the development of a new class of multifunctional sensors and actuators based on the application/removal of magnetic field without any temperature variation [1]. Besides the large MFIS [2-4], the MSMAs have received tremendous interest in the recent past due to the observation of several other exciting phenomena like the large magnetocaloric effect [5, 52-55], giant magnetoresistance [6, 57-59], anomalous thermal properties [7, 60], exchange bias effect [8, 61], spin-glass [9], giant Hall effect [12] and anomalous Nernst effect [13], all of which have great potential for technological applications. The study of the precursor PM phase in the MSMAs is of crucial importance in relation to several exotic phenomena like strain-glasses [10] and skyrmions [83].

Among the various MSMAs, the crystal structure, phase stability, and the magnetization behavior of the PM phase have been extensively investigated in the Ni-Mn-Ga system [63, 71, 88, 100, 104, 346]. For example, the temperature dependence of the dc magnetization in some of these alloys shows a small dip/peak at the PM transition [63, 100, 102] temperature at which it changes by ~2% as compared to that of the austenite phase [63, 97]. In contrast, the martensite phase transition is accompanied with a huge change (>40%) in magnetization [63, 97] due to large Bain distortion and therefore, much higher magnetocrystalline anisotropy of the martensite phase [326]. The PM phase of the near stoichiometric Ni_2MnGa is characterized by the appearance of very weak intensity satellite peaks in the diffraction pattern even as the cubic austenite phase peaks remain almost unaffected due to the absence of any discernible Bain distortion [63, 104]. As a result, the

PM phase has been regarded as a micro-modulated precursor state with preserved cubic symmetry [100]. This is in contrast to the martensite phase in which, besides the appearance of the new satellite peaks, cubic austenite peaks also split due to significant Bain distortion signaling a symmetry breaking transition [63, 104]. Recently, the evidence for the thermodynamic stability of both the PM and the martensite phases using a detailed temperature dependent synchrotron x-ray powder diffraction (SXRPD) study on Ni_2MnGa has been proposed [63].

The intermediate PM phase has been a subject matter of investigation in a few Ga-free Ni-Mn-X (X = Sn and In) MSMAs [83, 97, 347] also. For example, in Co-doped Ni-Mn-Sn alloys, obtained after pressure annealing [348, 349], the appearance of the precursor PM phase has been attributed to enhanced magnetoelastic coupling [97, 100, 102, 141]. Chemical pressure, generated by substitution with smaller size atoms, like Al at the In site in the Ni-Mn-In alloy composition, has also been reported to stabilize the PM phase over a modest temperature range of about 40 K [97]. The stabilization of the PM phase has also been reported in the conventional shape memory alloys like NiTi after partial substitution of Ni with Fe [106] and in Ni_xAl_{100-x} for $x < 60$ [105, 350], by chemical pressure tuning.

The foregoing results highlight the importance of chemical pressure-tuning of the transition temperature leading to the stabilization of the precursor PM phase and destabilization of the martensite phase. However, all these studies are mainly based on bulk magnetic measurements without any temperature dependent structural studies. Since the laboratory source x-ray powder diffraction data often fails to capture the signatures of the PM phase [351], any structural confirmation of the chemical pressure-tuned PM phase in MSMAs requires high-resolution SXRPD data, which not only reveal the presence of characteristic weak satellite peaks due to its high signal to noise ratio but also its ability to capture the Bain distortion, if present, and hence

the signature of the symmetry-breaking transition, unambiguously due to the high peak to peak resolution [63, 71, 85]. In the present chapter, a comprehensive study on the effect of the chemical pressure generated by Al substitution in place of In in $Ni_{50}Mn_{34}In_{16}$ (or $Ni_2Mn_{1.36}Al_{0.64}$) MSMA is carried out using bulk magnetic measurements, temperature dependent high-resolution SXRPD studies, and first-principles calculations. Our magnetic susceptibility studies on these alloys suggest that Al substitution in place of In destabilizes the martensite phase and stabilizes the PM phase over a wider temperature range. Our temperature dependent high-resolution SXRPD studies on these alloys reveal Bain distortion in the martensite phase and its absence in the PM phase. The bulk magnetic and structural studies show that Al free $Ni_{50}Mn_{35}In_{15}$ MSMA exhibits only the martensite phase of 3*M* type in the monoclinic space group *P*2/*m* with significant Bain distortion [91]. However, in the ~3% Al substituted $Ni_{50}Mn_{34}In_{15.5}Al_{0.5}$ alloy, a PM phase, stable over a narrow temperature window of ~10 K below the ferromagnetic T_C ~ 317 K, precedes the appearance of the martensite phase at lower temperatures. The PM to the martensite phase transition is shown to be an isostructural phase transition as both the phases are of 3*M* type in the monoclinic *P*2/*m* space group and differ only in terms of the absence or otherwise of the Bain distortion. More significantly, we show that on increasing the Al content to ~5% (i.e., $Ni_{50}Mn_{34}In_{15.2}Al_{0.8}$), only the PM phase, without any Bain distortion, occurs over the entire temperature range (300 K to 5 K) below the PM transition temperature T_{PM} ~ 300 K without any signature of the martensite phase transition either in the magnetic or the structural studies. We also show that the T_{PM} decreases with increasing magnetic field, and the satellite peaks of the PM phase disappear in the presence of an external magnetic field, confirming the magnetoelastic coupling in this alloy composition. Our results demonstrate that Al substituted Ni-Mn-In MSMAs provide an ideal platform for investigating the physics of PM phase-related phenomena in MSMAs.

5.2 Experimental Section

The polycrystalline alloys with ~3% and 5% Al substitution in place of In site in $Ni_{50}Mn_{34}In_{16}$ leading to nominal compositions $Ni_{50}Mn_{34}In_{15.5}Al_{0.5}$ and $Ni_{50}Mn_{34}In_{15.2}Al_{0.8}$, respectively, were prepared by the conventional arc-melting technique [266] under argon atmosphere using the appropriate quantity of each constituent element (99.99% purity). The samples were melted several times to get good homogeneity. An extra 2% manganese (Mn) was added before melting to compensate for the Mn loss due to its evaporation during melting. The melt-cast ingot was annealed in a vacuum-sealed quartz ampoule (vacuum ~10^{-6} mbar) at 800ºC for 24 h to achieve further homogeneity and then quenched in ice water. A part of the homogenized bulk sample was crushed into powder using a mortar pestle and sealed in quartz ampoule under the argon atmosphere (first evacuated up to ~10^{-6} mbar and then argon filled) followed by annealing at 500ºC for 12 h and finally furnace cooled to remove residual stresses [148, 267-269, 352], if any, introduced during the grinding. This stress-free annealed powder samples were used for all the characterizations. The chemical compositions were checked by the energy dispersive analysis of x-rays (EDAX) technique using EVO-Scanning Electron Microscope MA15/18 (SEM, ZEISS). The compositions so obtained are $Ni_{50.05}Mn_{33.93}In_{15.57}Al_{0.53}$ and $Ni_{51.9}Mn_{34.42}In_{12.76}Al_{0.81,}$ which correspond to $Ni_{50}Mn_{34}In_{15.5}Al_{0.5}$ (or $Ni_2Mn_{1.36}In_{0.62}Al_{0.02}$) and $Ni_{50}Mn_{34}In_{15.2}Al_{0.8}$ (or $Ni_2Mn_{1.36}In_{0.61}Al_{0.03}$), respectively. The backscattered electron (BSE) images of both the compositions were also recorded for the phase-contrast study. The differential scanning calorimetry (DSC) measurements were performed during heating and cooling cycles using DSC-60 plus (Mettler, M/s Shimadzu Pte Ltd.) in dynamic mode for phase transition study.

X-ray powder diffraction (XRD) data were collected using an 18-kW rotating Cu anode-based x-ray diffractometer (Rigaku) fitted with a curved graphite crystal monochromator in the diffraction beam. A closed-cycle He refrigerator-based low temperature attachment was used for XRD measurements in the 300 to 13 K range. In addition, high-resolution synchrotron x-ray powder diffraction (SXRPD) data were collected in the 400-100 K range at the temperature interval of 10 K in the cooling cycle at a wavelength of λ ~ 0.207 Å at P02.1 beamline of PETRA-III, DESY, Germany. The sample containing capillary was spinning continuously to minimize the texturing effect in the SXRPD data. Further, high-resolution SXRPD data were collected without and with magnetic field bias (0 Oe and 2500 Oe) at 294 K at a wavelength of λ ~ 0.495 Å on the Xpress beamline of ELETTRA, Italy [247]. A simple custom-made setup, based on a permanent magnet giving a field of ~2500 Oe at the sample, fitted to the beamline sample stage with the sample containing capillary in the center, was used for applying the magnetic field. The sample containing capillary was oscillated continuously to minimize the texturing effect in the SXRPD data collected at ELETTRA.

The temperature dependent ac-susceptibility ($\chi(T)$) at a drive field 10 Oe for 333.33 Hz frequency and dc magnetization ($M(T)$) data at 100 Oe were collected under zero-field cooled warming (ZFCW), field cooled (FC), and field cooled warming (FCW) protocols using a superconducting quantum interference device (SQUID) based magnetometer (Quantum Design, MPMPS-3). For the ZFCW protocol, the sample was cooled from 380 K (well above its ferromagnetic T_C) down to 5 K in the absence of magnetic field, and then the $\chi(T)$ and $M(T)$ data were collected up to 360 K during warming. Further, the data were also collected while cooling the sample under field (FC) and during the warming cycle on the field cooled sample (FCW). The magnetic field-dependent

isothermal magnetization (*M(H)*) and *M(T)* at several fields under the ZFCW protocol were collected using a VSM module equipped in a PPMS (Quantum Design).

5.3 Results and Discussion

5.3.1 Phase Purity and Phase Transition

Phase purity and crystal structure were confirmed by laboratory source XRD measurements. The average long-range ordered structure was confirmed by Le Bail refinement [353] using the powder x-ray diffraction patterns. All the refinements were carried out using the FULLPROF package [299]. For the Al ~ 3% composition with chemical formula $Ni_{50}Mn_{34}In_{15.5}Al_{0.5}$, the results of Le Bail refinement using XRD data at 300 K is shown in Figure 5.1(a), which reveals an excellent fit between observed and calculated profiles for the 3*M* modulated monoclinic structure (*P2/m* space group). The presence of multiple peaks around the most intense Bragg peak (inset of Figure 5.1(a)) suggests the Bain distorted martensite phase as reported in the Ni-Mn-In MSMA [91]. All the peaks related to the martensite phase ('M') around the most intense Bragg peak region are well indexed (see inset of Figure 5.1(a)). This suggests that $Ni_{50}Mn_{34}In_{15.5}Al_{0.5}$ MSMA exhibits martensite phase with 3*M* modulated monoclinic structure in the *P2/m* space group at 300 K. In contrast, for the Al ~ 5% composition ($Ni_{50}Mn_{34}In_{15.2}Al_{0.8}$), the Le Bail refinement using XRD data, shown in Figure 5.1(b), suggest the cubic austenite phase in the $Fm\bar{3}m$ at 300 K. The presence of (111) and (200) Bragg reflections shown in the inset of Figure 5.1(b) confirms the ordered $L2_1$ ordered cubic structure for the austenite phase [91]. The BSE images of $Ni_{50}Mn_{34}In_{15.5}Al_{0.5}$ and $Ni_{50}Mn_{34}In_{15.2}Al_{0.8}$ alloy are shown in Figure 5.1(c) and Figure 5.1(d), respectively. The BSE images show single contrast, apart from the thin line-like contrast, which arises due to scratches that appeared on the sample during its polishing. The presence of single contrast in the BSE image

further confirms the phase and compositional homogeneity of both $Ni_{50}Mn_{34}In_{15.5}Al_{0.5}$ and $Ni_{50}Mn_{34}In_{15.2}Al_{0.8}$ alloys.

To check the phase transitions, DSC measurements were carried out and the data is shown in Figure 5.2(a) and Figure 5.2(b) for $Ni_{50}Mn_{34}In_{15.5}Al_{0.5}$ and $Ni_{50}Mn_{34}In_{15.2}Al_{0.8}$, respectively. For the $Ni_{50}Mn_{34}In_{15.5}Al_{0.5}$ MSMA, the appearance of a sharp peak during cooling and sharp dip during heating indicate the martensite and reverse martensite phase transition, respectively (see Figure 5.2(a)), as generally observed in Ni-Mn-In MSMA [97]. In contrast, a tiny peak during cooling (or dip during heating) indicate that this transition is related to the paramagnetic to ferromagnetic (FM) phase transition (i.e., not related with martensite phase transition) in $Ni_{50}Mn_{34}In_{15.2}Al_{0.8}$ MSMA (see Figure 5.2(b)), as reported in Ni-Mn-In MSMA [97].

In order to confirm the magnetic correlation at low temperature, the magnetic field dependent isothermal magnetizations (*M(H)* loop) were collected. The *M(H)* loop at 5 K of $Ni_{50}Mn_{34}In_{15.5}Al_{0.5}$ MSMA is shown in Figure 5.2(c), which reveals a low value of saturation magnetization ($M_S \sim 1.5\ \mu_B$/f.u.). In general, such a low value of M_S is observed in the martensite phase of Ni-Mn-In MSMA, for e.g., $M_S \sim 1.5\ \mu_B$/f.u. at 2 K for $Ni_{50}Mn_{35}In_{15}$ MSMA [91], due to competition between ferromagnetic and antiferromagnetic (AFM) interactions [96, 354]. In contrast, the *M(H)* loop at 2 K of $Ni_{50}Mn_{34}In_{15.2}Al_{0.8}$ MSMA (shown in Figure 5.2(d)) reveals a typical ferromagnetic character with a high value of saturation magnetization ($M_S \sim 5.82\ \mu_B$/f.u.). Such a large value of M_S (~ 5.82 μ_B/f.u.) for $Ni_{50}Mn_{34}In_{15.2}Al_{0.8}$ is comparable to the M_S (~ 6.17 μ_B/f. u.) observed in the austenite phase of $Ni_{50}Mn_{35}In_{15}$ MSMA, which do not contain martensite phase transition [290]. This indicates the absence of the martensite phase transition down to 2 K in $Ni_{50}Mn_{34}In_{15.2}Al_{0.8}$ alloy.

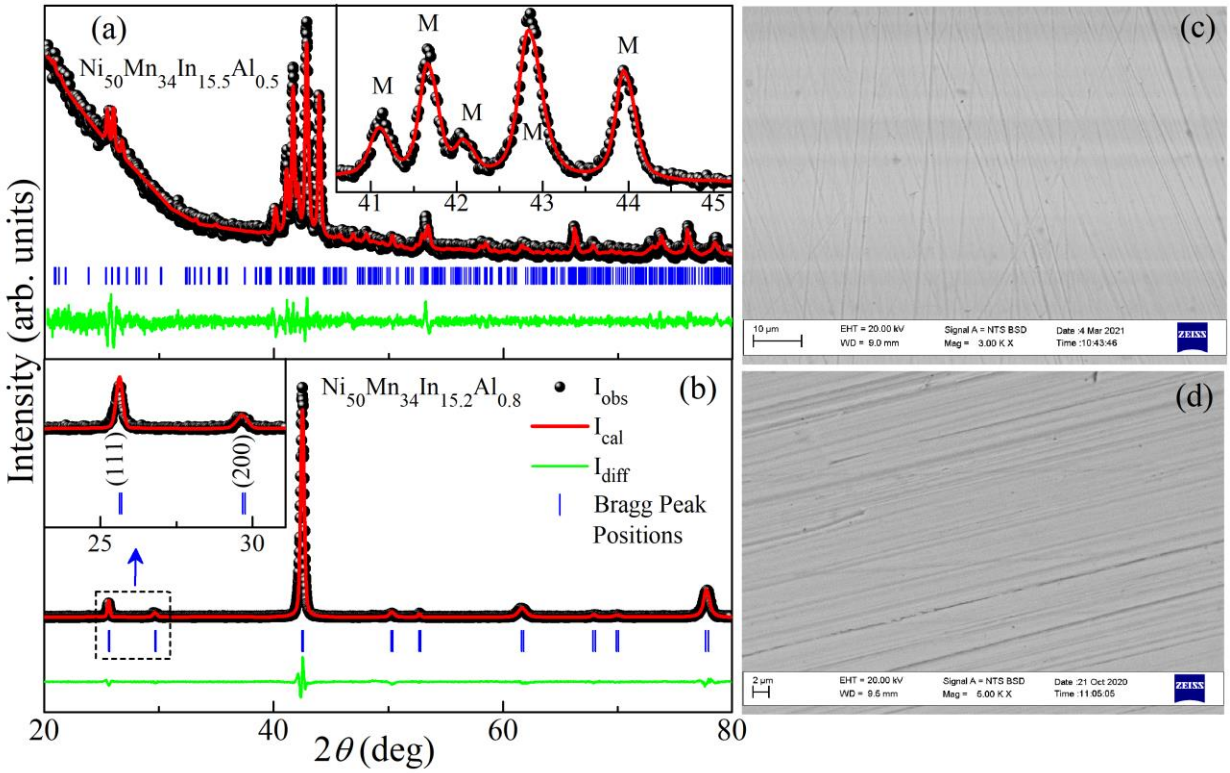

Figure 5.1: The observed (dark black dots), calculated (continuous red line), and difference profiles (continuous green line) obtained after Le Bail refinement using laboratory source XRD data at 300 K for (a) the martensite phase in the *P*2/*m* space group for $Ni_{50}Mn_{34}In_{15.5}Al_{0.5}$ and (b) for the cubic austenite phase in the $Fm\bar{3}m$ space group for $Ni_{50}Mn_{34}In_{15.2}Al_{0.8}$. Above the difference profile, the vertical tick marks represent the Bragg peak positions in (a) and (b). The inset of (a) depicts an enlarged view of fit around the most intense Bragg peak, while the inset of (b) shows an enlarged view of fit around the (111) and (200) Bragg reflections. The BSE image for (c) $Ni_{50}Mn_{34}In_{15.5}Al_{0.5}$ and (d) $Ni_{50}Mn_{34}In_{15.2}Al_{0.8}$.

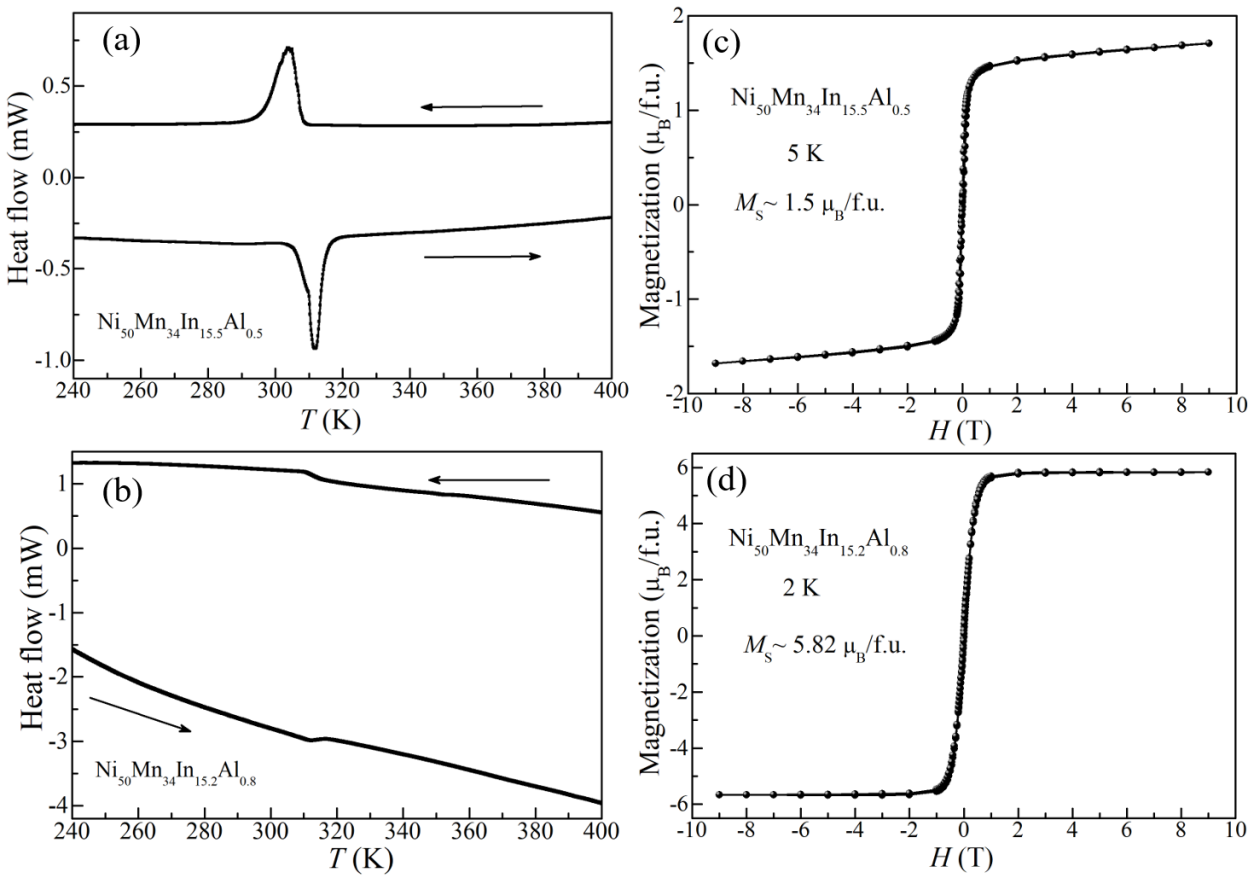

Figure 5.2: The DSC data for (a) $Ni_{50}Mn_{34}In_{15.5}Al_{0.5}$ and (b) $Ni_{50}Mn_{34}In_{15.2}Al_{0.8}$. The arrows in (b) and (c) indicate the heating and cooling cycle. The magnetic field dependent magnetization ($M(H)$ loop) for (c) $Ni_{50}Mn_{34}In_{15.5}Al_{0.5}$ at 5 K and (d) $Ni_{50}Mn_{34}In_{15.2}Al_{0.8}$ at 2 K. The value of saturation magnetic moment (M_S) is indicated in (c) and (d).

5.3.2 Magnetization and High-Resolution Synchrotron X-ray Powder Diffraction

The Al-free $Ni_{50}Mn_{35}In_{15}$ (or $Ni_2Mn_{1.4}In_{0.6}$) MSMA [91] exhibits paramagnetic to ferromagnetic (FM) transition with T_C ~ 315 K, a first-order austenite to martensite transition in the FM phase at T_M ~ 295 K with a characteristic thermal hysteresis in the temperature dependent magnetization *M(T)* plots for the field cooled (FC) and field cooled warming (FCW) protocols and another transition at T_C^M ~150 K, commonly attributed to competing FM and AFM interactions [96, 354, 355], with the bifurcation of the zero-field cooled warming (ZFCW) and FC *M(T)* plots in the dc

magnetization studies [91]. While the FM T_C of the base alloy ($Ni_{50}Mn_{35}In_{15}$) is known to be nearly unaffected by Al substitution [58, 97], the nature of transitions below T_C changes rather drastically as a function of Al content. This can be seen from a comparison of magnetization data shown in Figure 5.3(a) of the base alloy in ref. [91] with those given in Figure 5.3(b) and Figure 5.3(c). For the ~3% Al substituted composition ($Ni_{50}Mn_{34}In_{15.5}Al_{0.5}$), we observed two peaks at T_{PM} ~ 311 K and T_M ~ 300 K in the real part of ac-susceptibility ($\chi'(T)$) plot shown in the inset of Figure 5.3(b) corresponding to the premartensite and martensite transitions, respectively. Both the transitions exhibit characteristic thermal hysteresis in $\chi'(T)$ plots for the FC and FCW protocols, shown in the main figure (Figure 5.3(b)), suggesting their first-order character. The nature of the two transitions shown in Figure 5.3(b) are in broad agreement with those reported in a previous study [97, 347], even though the transition temperatures and behavior of $\chi'(T)$ are somewhat different, possibly due to a small fluctuation in the alloy composition [37, 56, 96, 356, 357].

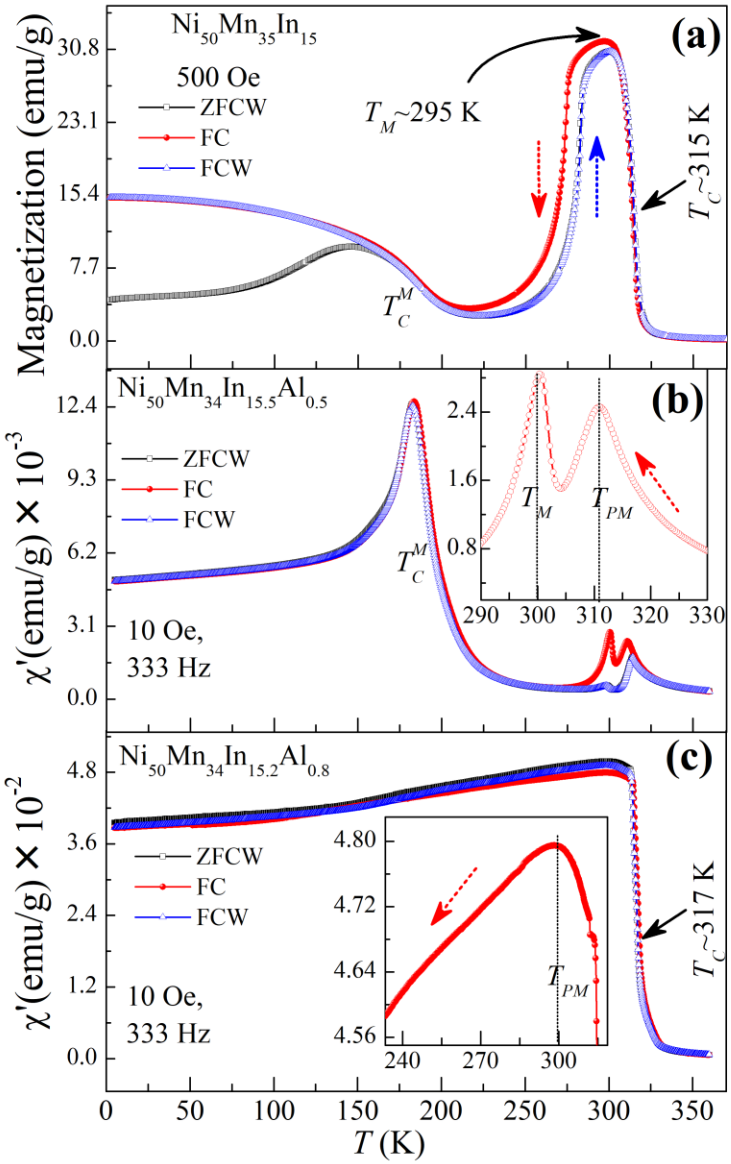

Figure 5.3: (a) The temperature dependent dc-magnetization at 500 Oe for Al free $Ni_{50}Mn_{35}In_{15}$ (taken from reference [91]). The temperature dependent real part of ac-susceptibility for (b) $Ni_{50}Mn_{34}In_{15.5}Al_{0.5}$ and (c) $Ni_{50}Mn_{34}In_{15.2}Al_{0.8}$ MSMAs. The insets are enlarged view around 300 K for the field cooled protocol. The T_M, T_{PM}, T_C^M and T_C represent the martensite transition temperature, premartensite transition temperature, Curie temperature of the martensite phase, and Curie temperature of the austenite phase, respectively. The ZFCW, FC, and FCW correspond to measurements performed during warming on the zero-field cooled sample, during field cooling, and during warming on the field cooled sample, respectively.

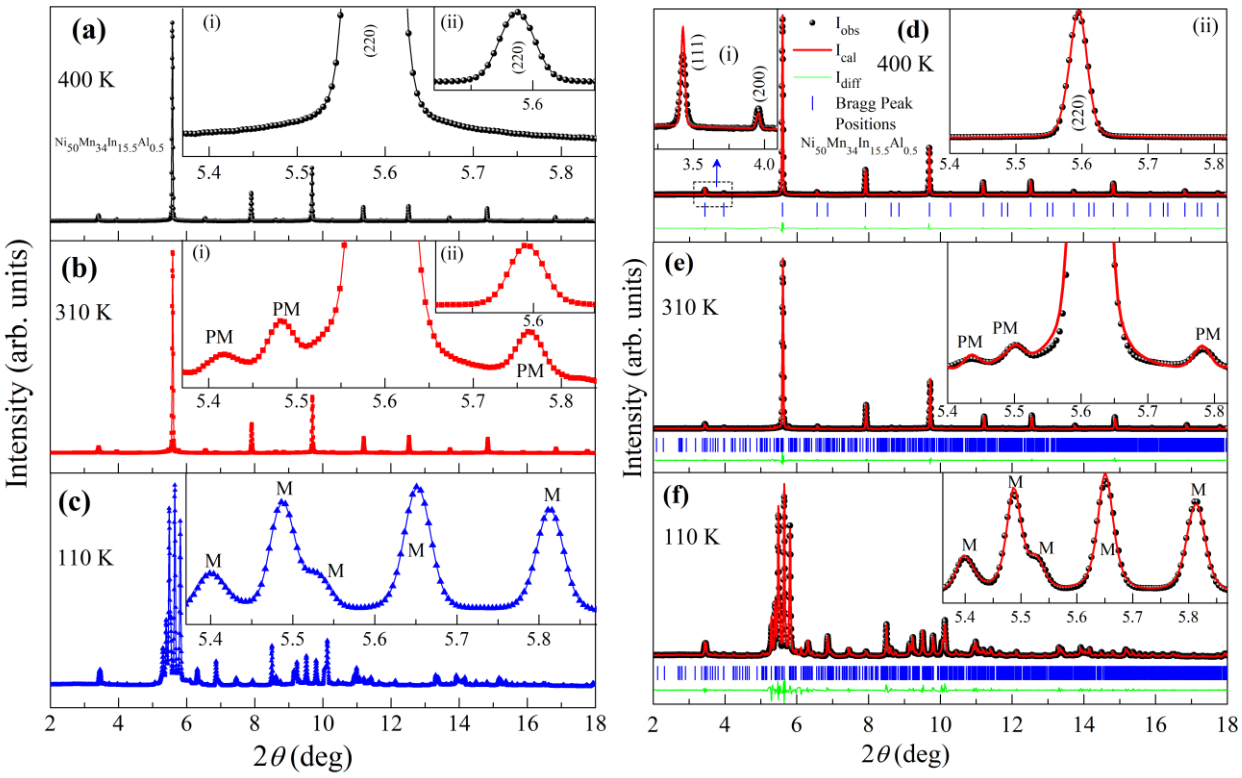

Figure 5.4: Typical SXRPD patterns of $Ni_{50}Mn_{34}In_{15.5}Al_{0.5}$ MSMA in the (a) austenite, (b) premartensite, and (c) martensite phases. An enlarged view around the most intense (220) Bragg peak for the austenite and the premartensite (PM) phases, given in inset (i) of (a) and (b), respectively, reveal the appearance of the satellite peaks (indicated by 'PM' in the inset (i) of (b)) due to 3*M* like modulation in the PM phase. Untruncated view of the (220) cubic peak for the austenite and PM phases, given in inset (ii) of (a) and (b), respectively, reveal the absence of Bain distortion in the PM phase. The inset of (c) depicts the splitting of the most intense (220) cubic peak and appearance of the satellite peaks due to Bain distortion and 3*M* like modulation of the martensite (M) phase. The observed (dark black dots), calculated (continuous red line), and difference patterns (continuous green line), obtained after Le Bail refinement using the SXRPD data for the (d) cubic austenite, (e) 3M modulated PM, and (f) 3*M* modulated martensite phases in the $Fm\bar{3}m$, *P2/m*, and *P2/m* space groups, respectively, for $Ni_{50}Mn_{34}In_{15.5}Al_{0.5}$. The vertical ticks above the difference profile represent the Bragg peak positions. The insets (i) and (ii) of (a) show an enlarged view of fit around the (111) and (200) Bragg reflections and around the most intense Bragg peak, respectively. The inset of (e) and (f) shows fits around the most intense Bragg peak region in a magnified scale. The satellite peaks of the PM phase are marked as 'PM' at 310 K in

the inset of (b) and (e). The peaks related to the martensite phase are marked as 'M' at 110 K in the inset of (c) and (f).

We now proceed to correlate the two anomalies in $\chi'(T)$ of $Ni_{50}Mn_{34}In_{15.5}Al_{0.5}$ with premartensite and martensite phase transitions using structural studies. Figure 5.4(a), (b), and (c) depict the SXRPD patterns of $Ni_{50}Mn_{34}In_{15.5}Al_{0.5}$ recorded at 400 K ($> T_C$), 310 K, and 110 K, respectively. The emergence of new peaks in these SXRPD patterns at 310 and 110 K reveal structural changes related with the premartensite and martensite transitions, respectively. All the peaks in Figure 5.4(a) can be indexed with the austenite cubic structure in the $Fm\bar{3}m$ space group, as confirmed by Le Bail refinement, which is given in Figure 5.4(d). The cubic lattice parameter obtained after the refinement is found to be a = 6.01009(6) Å. Further, the presence of the (111) and (200) Bragg reflections (see the inset (i) of Figure 5.4(d)) confirms the $L2_1$ ordering above the FM T_C ~ 317 K. At T ~ 310 K ($< T_{PM}$), new satellite peaks with very low intensities appear, as can be seen from the inset (i) of Figure 5.4(b), which gives the SXRPD plot on a magnified scale for a limited 2θ-range. All the peaks, including the satellite peaks, in this pattern, are well accounted by a 3M modulated monoclinic structure in the $P2/m$ space group with a = 4.3869(7) Å, b= 5.6866(1) Å, c =13.0028(2) Å and β = 93.695(3)^o as can be seen from Figure 5.4(e) which gives the results of Le Bail refinement for the SXRPD pattern at ~310 K. At this temperature, the "cubic" peaks do not show any splitting (see inset (ii) of Figure 5.4(b)) confirming the appearance of the PM phase below T_{PM} with preserved cubic symmetry without any discernible Bain distortion, similar to the PM phase of Ni_2MnGa [71, 123]. On lowering the temperature further below T_M, the intensity of the existing satellite peaks increases considerably while the "cubic" peaks split into multiple peaks (see the inset of Figure 5.4(c) due to significant Bain distortion, as expected for the martensite phase [91].

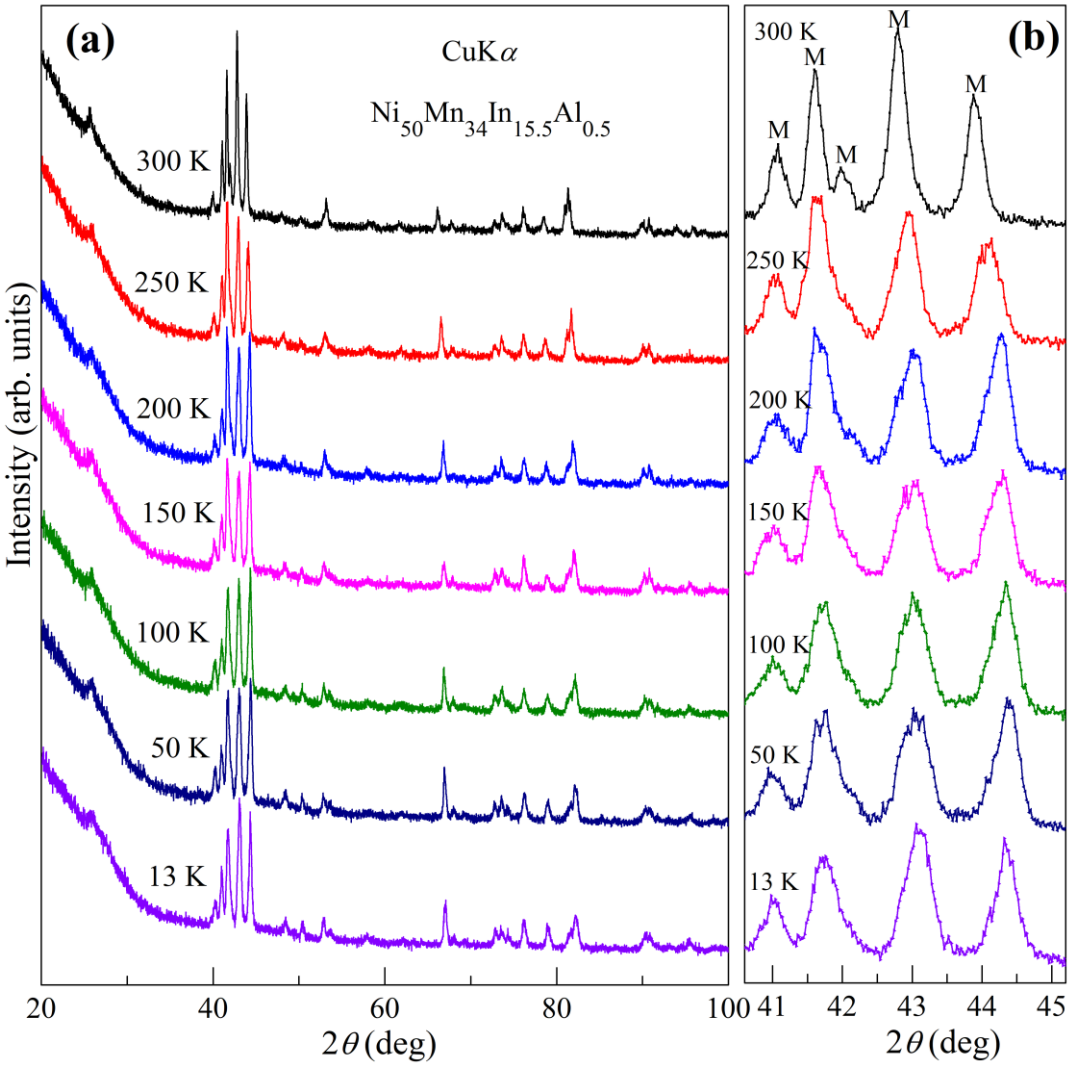

Figure 5.5: (a) The laboratory source (CuKα) XRD data at indicated temperature (300 to 13 K) for $Ni_{50}Mn_{34}In_{15.5}Al_{0.5}$ MSMA. (b) An enlarged view around the most intense Bragg peak region of (a). The peaks related to the martensite phase are marked as 'M' in (b).

Le Bail refinement for the 110 K SXRPD pattern confirms that all the peaks in the martensite phase are also accounted for using the monoclinic *P2/m* space group (see Figure 5.4(f)). The stability of the martensite phase is also verified from 300 K down to 13 K using x-ray powder diffraction data obtained from an 18 kW Cu rotating anode-based high-resolution diffractometer fitted with a curved graphite crystal monochromator in the diffraction beam and a closed-cycle He

refrigerator-based low-temperature attachment. The corresponding x-ray diffraction (XRD) patterns in the 20 to 100º 2θ-range are depicted in Figure 5.5(a), whose enlarged view around the most intense Bragg peak region is shown in Figure 5.5(b). Thus, the SXRPD studies on the $Ni_{50}Mn_{34}In_{15.5}Al_{0.5}$ alloy above 300 K unleashes the cubic austenite to monoclinic (space group $P2/m$) PM phase transition at T_{PM} without any Bain distortion, as revealed by the absence of any splitting of the "cubic" peaks, while the SXRPD shows an isostructural PM to martensite phase transition with significant Bain distortion, as evident by the splitting of the "cubic" peaks in the martensite phase.

On increasing the Al content from ~3% to ~5% (i.e., $Ni_{50}Mn_{34}In_{15.2}Al_{0.8}$ MSMA), the phase transition behavior changes drastically. Figure 5.3(c) shows the temperature dependence of the real part of $\chi'(T)$ for ~5% Al substituted alloy, $Ni_{50}Mn_{34}In_{15.2}Al_{0.8.}$ For the FC protocol, the paramagnetic to FM transition occurs at T_C ~ 317 K with a sharp increase in the $\chi'(T)$, comparable to the T_C of the base alloy as can be seen from a comparison of Figure 5.3(c) with the temperature dependence of dc magnetization of the base alloy (Figure 5.3(a)) in ref. [91]. On decreasing the temperature further, the rate of increase of $\chi'(T)$ decreases before peaking at the PM transition temperature T_{PM} ~ 300 K, as can be seen from the inset of Figure 5.3(c). This peak is highly skewed and smeared out on the lower temperature side down to ~5 K. The gradually decreasing trend of $\chi'(T)$ below T_{PM} is in marked contrast to its sharp drop in dc magnetization of the base alloy [91], which is usually attributed to a very large magnetocrystalline anisotropy of the martensite phase [326]. More significantly, there is no signature of the second anomaly, seen in Figure 5.3(b) for $Ni_{50}Mn_{34}In_{15.5}Al_{0.5}$, corresponding to the martensite transition in $Ni_{50}Mn_{34}In_{15.2}Al_{0.8}$.

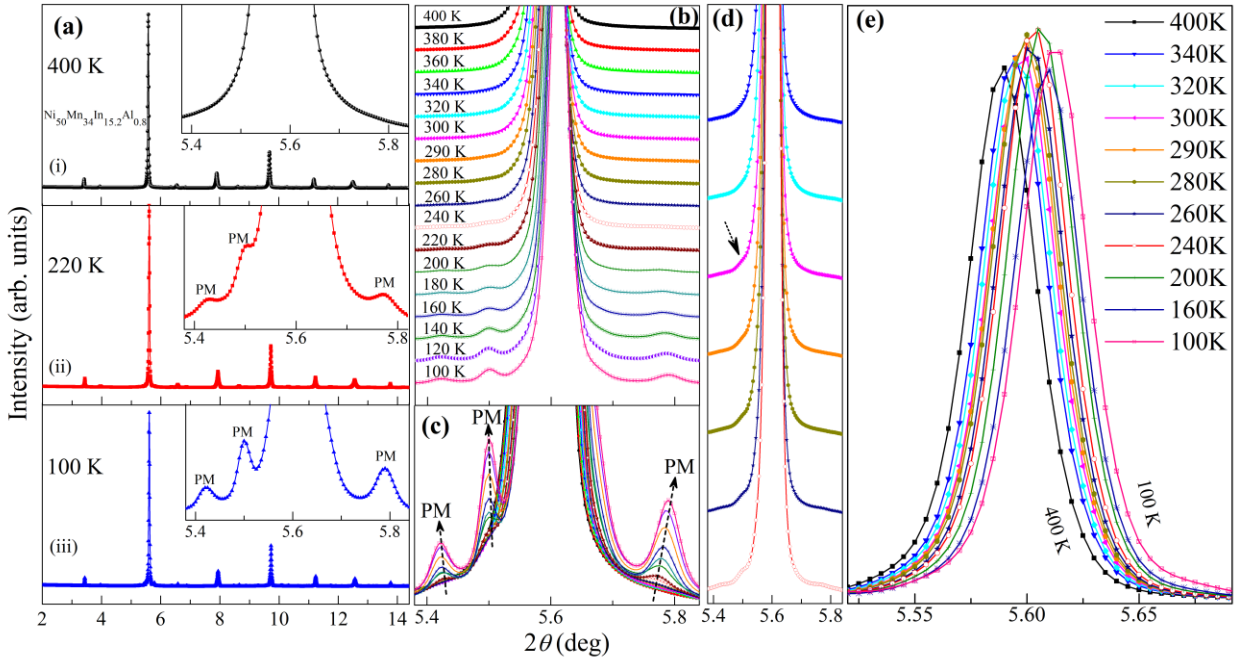

Figure 5.6: The SXRPD patterns of $Ni_{50}Mn_{34}In_{15.2}Al_{0.8}$ are shown in (a) at (i) 400 K, (ii) 220 K, and (iii) 100 K. The insets show an enlarged view around the most intense Bragg peak to reveal the satellite peaks of the premartensite (PM) phase. The enlarged view around the most intense cubic peak (220) at the various temperatures in the range 400-100 K are given in (b) and (c). The arrows in (c) indicate the temperature dependent shifts of the PM satellite peak positions. Note the gradual sharpening of the satellite peaks in (c) on lowering the temperature. (d) An enlarged view around the most intense (220) cubic peak at selected temperatures reveal the appearance of the most intense satellite peak of the PM phase at T ~ 300 K, indicated by an arrow. (e) Untruncated SXRPD profiles of the (220) cubic Bragg peak is depicted in the 400 to100 K range. The satellite peaks of the PM phase are marked as 'PM' in the inset of (ii) and (iii) of (a) and in (c).

The absence of martensite transition and stabilization of the PM phase indicated by the $\chi'(T)$ plot in Figure 5.3(c) was confirmed by SXRPD studies at selected temperatures in the 400 to 100 K range and laboratory source XRD patterns at several temperatures in the 300 to 13 K range. Figure 5.6(a) compares the SXRPD patterns of $Ni_{50}Mn_{34}In_{15.2}Al_{0.8}$ alloy at 400, 220, and 100 K. The insets in panels (i), (ii), and (iii) depict a magnified view of the profiles in the 2θ range 5.38º to

5.84º around the most intense Bragg peak. The inset of (ii) reveals the presence of satellite peaks at 220 K, whose intensity increases on lowering the temperature to 100 K (see inset of (iii)).

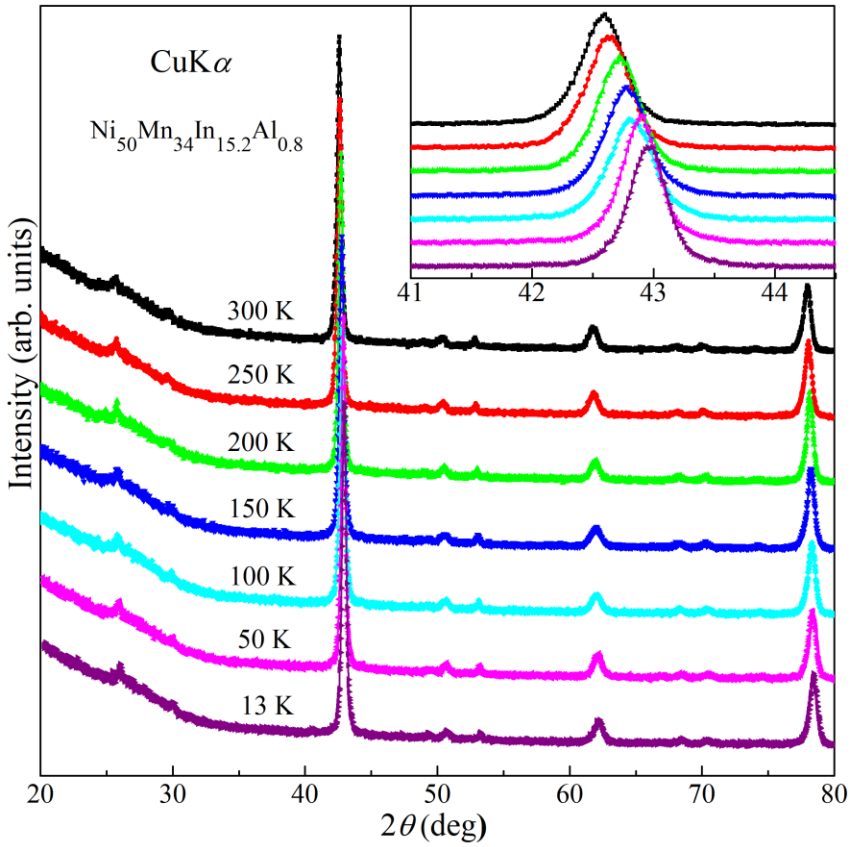

Figure 5.7: The laboratory source (CuKα) XRD data of $Ni_{50}Mn_{34}In_{15.2}Al_{0.8}$ alloy at indicated temperatures (300 to 13 K) wherein the inset shows an enlarged view around the most intense Bragg peak.

These satellite peaks are absent at 400 K, as can be seen in the inset of (i). The evolution of the SXRPD profiles as a function of temperature are shown in Figure 5.6(b) and (c) at close temperature intervals using a magnified (vertically zoomed) view of the intensity profile around the most intense cubic (220) peak. The most intense satellite appears around 300 K as shown with an arrow in Figure 5.6(d), in agreement with the transition temperature T_{PM} corresponding to the

austenite to PM transition in the $\chi'(T)$ plot shown in Figure 5.3(c). The intensity of the three prominent satellite peaks around the (220) cubic peak keeps growing below 300 K, as can be seen from Figure 5.6(b) and (c). Further, the FWHM of the satellite peaks decreases (see Figure 5.6(c)) with decreasing temperature, suggesting that the correlation length or the domain size of the PM phase keeps growing below 300 K after its nucleation around T_{PM} = 300 K. Moreover, the cubic (220) peak does not show any splitting down to the lowest temperature 100 K up to the SXRPD patterns could be collected (see Figure 5.6(e)). The absence of splitting in this peak even below 100 K is verified using the laboratory source XRD data. The temperature dependent laboratory source XRD patterns for $Ni_{50}Mn_{34}In_{15.2}Al_{0.8}$ alloy are shown in Figure 5.7, wherein the inset depicts an enlarged view of the most intense (220) Bragg peak. The absence of any splitting of the (220) cubic peak, shown in Figure 5.7, down to 13 K is in marked contrast to that shown in Figure 5.5(b) for $Ni_{50}Mn_{34}In_{15.5}Al_{0.5}$ alloy. This confirms the stability of the PM phase down to 13 K with preserved cubic symmetry without any discernible Bain distortion. The absence of any splitting of the (220) austenite peak, the appearance of the satellite peaks at $T \leq T_{PM} \sim 300$ K and the absence of any peak in the $\chi'(T)$ plot in Figure 5.3(c) below the T_{PM} corresponding to the martensite transition clearly confirm the suppression of the martensite phase in $Ni_{50}Mn_{34}In_{15.2}Al_{0.8}$ and the stabilization of the PM phase in the entire temperature range below T_{PM}. These qualitative observations were verified by Le Bail refinements of SXRPD data as discussed below.

The Le Bail refinement using the SXRPD pattern at 400 K (Figure 5.8(a)) for the $Ni_{50}Mn_{34}In_{15.2}Al_{0.8}$ alloy for the cubic austenite phase in the space group $Fm\bar{3}m$ confirmed that all the peaks in the SXRPD pattern could be indexed very well. The results of this refinement are shown in Figure 5.8(a), which reveals an excellent fit between the observed and calculated profiles for the refined unit cell parameter a = 6.0169(1) Å. The presence of (111) and (200) Bragg peaks

shown in the inset of Figure 5.8(a) confirms the ordered $L2_1$ cubic structure for the austenite phase [91]. Having confirmed the single-phase nature and $L2_1$ ordering in the cubic austenite phase of $Ni_{50}Mn_{34}In_{15.2}Al_{0.8}$, Le Bail refinement using the SXRPD pattern was carried out at 100 K (i.e., well below T_{PM}) for the 3*M* modulated monoclinic structure in the space group *P*2/*m*, similar to that for the $Ni_{50}Mn_{34}In_{15.5}Al_{0.5}$ composition. The observed, calculated, and difference profiles so obtained, shown in Figure 5.8(b), reveal an excellent fit for the 3*M* modulated monoclinic structure.

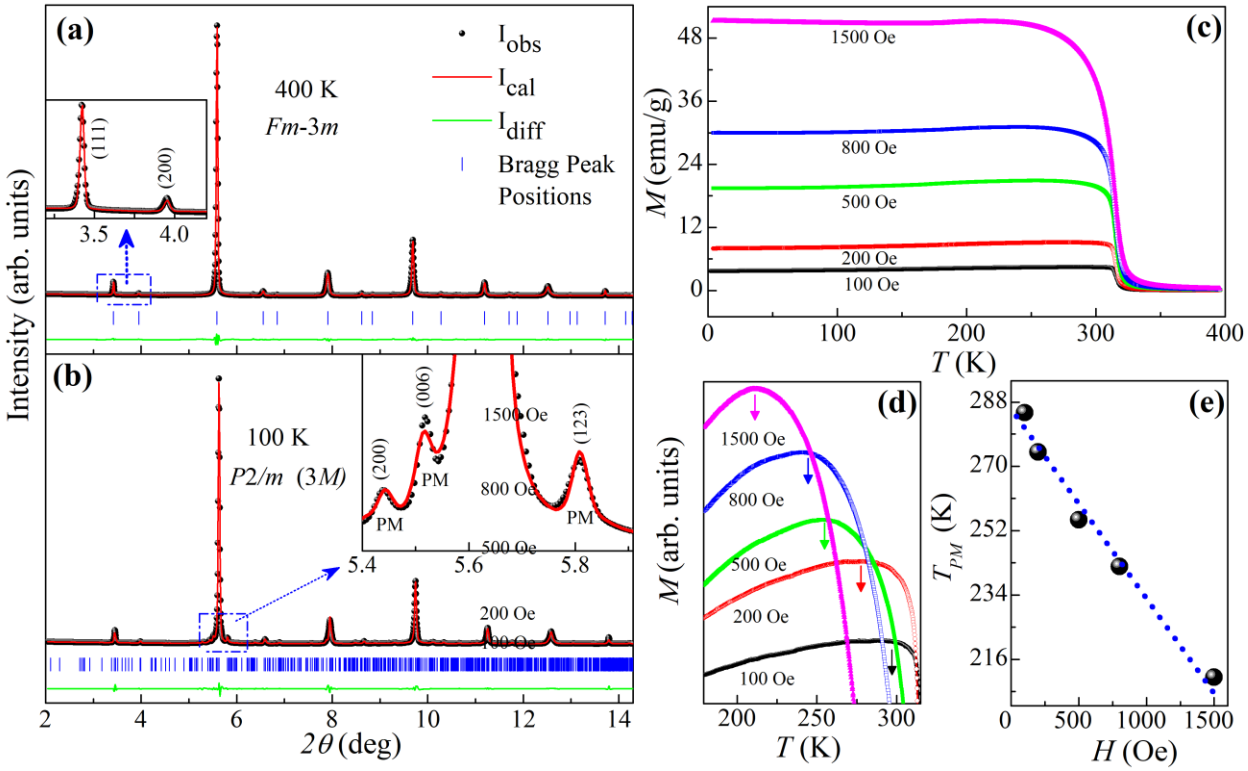

Figure 5.8: The observed (dark black dots), calculated (continuous red line), and difference patterns (continuous green line) obtained after Le Bail refinement using SXRPD pattern of $Ni_{50}Mn_{34}In_{15.2}Al_{0.8}$ MSMA for the (a) cubic austenite phase at 400 K and (b) 3*M* modulated premartensite (PM) phase at 100 K in the $Fm\bar{3}m$ and *P*2/*m* space groups, respectively. The vertical tick marks above the difference profile represent the Bragg peak positions in (a) and (b). The inset of (a) shows the presence of (111) and (200) Bragg reflections characteristic of the $L2_1$ ordering in the cubic austenite phase. The inset of (b) shows an enlarged view of the fit around the most

intense Bragg peak and satellite reflections (marked as 'PM' with their indices) related to the 3*M* modulated PM phase. The temperature dependence of the dc magnetization, measured on zero-field cooled sample during warming cycle, is shown in (c) for different magnetic fields. The enlarged view of (c) around the FM T_C, shown in (d), reveals a skewed diffuse peak due to the PM transition. The variation of the PM transition temperature (T_{PM}) with the magnetic field is shown in (e).

The inset of Figure 5.8(b) depicts an enlarged view of the Le Bail fit around the most intense Bragg peak. The satellite peaks corresponding to the PM phase are marked as 'PM' along with their indices in this inset. The refined lattice parameters obtained after refinements are (a = 4.3823(2) Å, b = 5.6480(4) Å, c = 12.9754(4) Å, β = 93.755(3)º) for the PM structure of $Ni_{50}Mn_{34}In_{15.2}Al_{0.8}$ at 100 K. These parameters correspond to the 3*M* modulated monoclinic structure as per the convention used in the literature for the modulated structures in MSMAs [38, 66, 70, 104, 358, 359].

The magnetoelastic coupling has been suggested as one of the factors for the stabilization of the PM phase in MSMAs [64, 97, 100, 348]. The effect of magnetoelastic coupling is manifested through the variation of T_{PM} with magnetic field [97, 100, 102, 348]. Therefore, to investigate the possibility of magnetoelastic coupling in $Ni_{50}Mn_{34}In_{15.2}Al_{0.8}$ MSMA, the temperature dependence of the dc magnetization as a function of temperature (*M(T)*) at different magnetic fields (100 Oe, 200 Oe, 500 Oe, 800 Oe, and 1500 Oe) is performed during warming cycle on zero-field cooled sample (ZFCW protocol) as shown in Figure 5.8(c). The enlarged view of Figure 5.8(c) around the diffuse peak in the *M(T)* is shown in Figure 5.8 (d), where the peak temperatures are marked by arrows. The variation of the peak temperatures in *M(T)* with the field, shown in Figure 5.8(e), reveals that T_{PM} shifts towards the lower temperature side linearly with the increasing magnetic field. This has been attributed to magnetoelastic coupling [97, 100, 102, 348].

We verified the magnetoelastic coupling in $Ni_{50}Mn_{34}In_{15.2}Al_{0.8}$ further by recording high-resolution SXRPD patterns without and in the presence of magnetic field (0 Oe and 2500 Oe) at 294 K. The results of such measurements are shown in Figure 5.9(a), wherein the inset depicts an enlarged view of the lower 2θ-range. An enlarged view of Figure 5.9(a) around the most intense Bragg peak is shown in Figure 5.9(b). The '*' in the inset of Figure 5.9(a) indicates the extra peaks related to the setup of magnets, which is shown in Figure 5.9(c). It is evident from Figure 5.9(b) that the satellite peaks related to the PM phase (marked as 'PM' for the zero-field pattern) disappear completely at 2500 Oe.

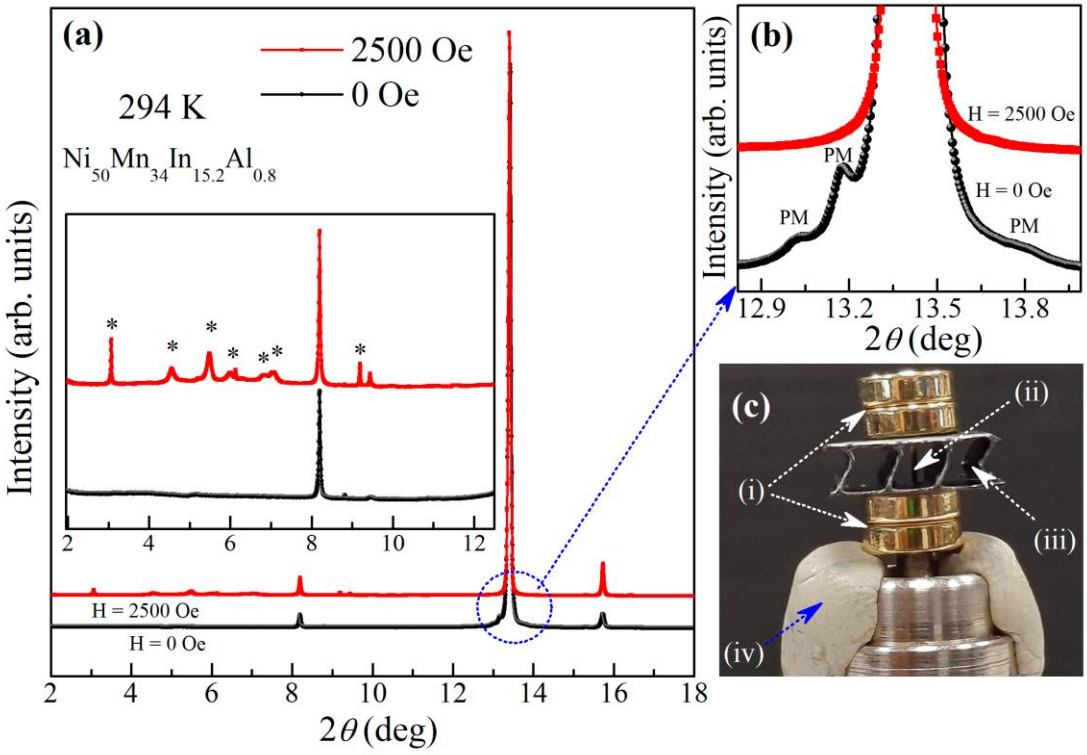

Figure 5.9: (a) High-resolution SXRPD pattern collected at 294 K under zero magnetic field (black dots connected with a continuous line) and an external magnetic field of 2500 Oe (red squares connected with a continuous line) for $Ni_{50}Mn_{34}In_{15.2}Al_{0.8}$. The inset of (a) shows an enlarged view of the lower 2θ-range (2-12.5°). (b) An enlarged view of encircled region of (a) (guided by arrow). Note the disappearance of the satellite peaks related to the premartensite (PM) phase under the

magnetic field. (c) Image of magnets setup used in measurement, where (i), (ii), (iii), and (iv) indicate the magnets, capillary position, plastic for support, and clay for positioning the magnets centered with respect to the capillary, respectively (shown by arrow). The '*' in the inset of (a) and 'PM' in (b) indicate the extra peaks related to the setup of magnets and satellite peaks related to the PM phase, respectively.

This confirms that the lattice and spin degrees of freedom are not only coupled but also play a crucial role on the stability of the PM phase of $Ni_{50}Mn_{34}In_{15.2}Al_{0.8}$ MSMA. The complete suppression of satellite peak related to the PM phase under the magnetic field (Figure 5.9(b)) provides direct evidence of magnetoelastic coupling in $Ni_{50}Mn_{34}In_{15.2}Al_{0.8}$ MSMA. It is worth mentioning here that the satellite peaks related to the PM phase are better resolved in Figure 5.9(b) than Figure 5.6(b) due to better peak to peak resolution for the lower energy (25 keV) beam used for the former in contrast to 60 keV beam used for the latter. Our theoretical calculations [360] also support the present experimental findings of stabilization of the PM phase with increasing Al content on the place of In and the crucial role of spin-lattice coupling on the stability of the PM phase in Ni-Mn-In MSMA.

5.4 Conclusions

To conclude, we presented the evidence for chemical pressure-induced suppression of the main martensite transition and stabilization of the PM phase over a very wide temperature range from around 300 K to 5 K in $Ni_{50}Mn_{34}In_{16}$ MSMA using magnetic susceptibility and synchrotron x-ray powder diffraction studies. The ac-susceptibility studies show that the stability of the martensite phase is suppressed while that of the premartensite phase is enhanced with increasing Al content in place of In in $Ni_{50}Mn_{34}In_{16}$. The temperature evolution of the SXRPD patterns confirmed the appearance of the PM phase-related satellite peaks at $T \leq 300$ K without any splitting of the main

austenite (220) peak, showing preserved cubic symmetry in ~5% Al substituted compositions ($Ni_{50}Mn_{34}In_{15.2}Al_{0.8}$). This was in marked contrast to the temperature evolution of the SXRPD patterns of the martensite phase of the Al free as well as ~3% Al substituted compositions ($Ni_{50}Mn_{34}In_{15.5}Al_{0.5}$), where the austenite (220) peak showed a clear splitting due to Bain distortion/symmetry breaking transition. Thus, our results suggest that the substitution at the In site by a smaller size atom, like Al, can stabilize the PM phase in Ni-Mn-In MSMAs. We have also shown that the T_{PM} decreases with the increasing magnetic field, indicating the role of magnetoelastic coupling. The disappearance of the satellite peaks of the PM phase in the SXRPD pattern in the presence of an external magnetic field provides direct evidence for the crucial role of magnetoelastic coupling in the stabilization of the PM phase in the base and ~5% Al substituted alloy compositions. Our results, thus, put forward Al-substituted Ni-Mn-In MSMA as an ideal system for investigating the physics of precursor phenomena in MSMAs.